

Effects of Acoustic Waves on Optical Wavefronts in Flight on AAOL-T

Nicholas De Lucca¹, Stanislav Gordeyev.² And Eric Jumper³

University of Notre Dame, Notre Dame, IN, 46556

and

Donald J. Wittich⁴

Air Force Research Laboratory, Directed Energy Directorate, Kirtland AFB, NM 87117

Wavefront measurements were performed for a hemispherical turret on the Airborne Aero-Optics Laboratory-Transonic (AAOL-T). For turret side-looking angles near 90°, upstream propagating wavefronts were observed. These wavefronts were contributed to acoustic waves originating from the engine downstream. These acoustical waves were modeled using combined potential flow solutions for a single-frequency moving acoustic source and a flow around a sphere. The model was shown to properly predict the spatial statistics and convective speeds of the experimentally-observed wavefronts. The model also correctly explained the viewing angle-dependence of the acoustic-related wavefronts.

I. Introduction

DIRECTED energy and free-space communications systems that can be operated on aircraft are desirable. To maximize the field of regard of these systems, hemispherical turrets are often used. As such, turrets have been studied extensively in the last decade in terms of both aerodynamic [1,2,3] and aero-optic [4,5,6] performance. Additionally there have been extensive CFD studies into the flow around hemispherical turrets [7,8,9,10,11].

The Airborne Aero-optics Laboratory, AAOL, and its current predecessor, AAOL-T, see Figure 1, is a flight test platform to study aero-optics [12,13]. It has been and still is a very instrumental program to collect extensive amount of experimental, realistic flight data around aero-optical environment for various turret configurations at various Mach Numbers between 0.4 and 0.8 [4,5,6], as well as to study effects of flow control devices on aero-optical performance [14]. The collected data is widely used by government agencies and private companies to understand the aero-optical performance of turret-based systems and to design and develop future airborne systems for various applications.



Figure 1: AAOL-T laboratory aircraft with a hemispherical turret installed.

¹ Graduate Research Assistant, Department of Aerospace and Mech. Eng., Student AIAA Member

² Associate Professor, Department of Aerospace and Mech. Eng., AIAA Associate Fellow

³ Professor, Department of Aerospace and Mech. Eng., AIAA Fellow

⁴Aerospace Engineer, Laser Division, 3550 Aberdeen Ave SE.

Given the importance of the flight data, it is crucial to understand and address the sources of differences between the flight data and the tunnel data, as well as various contaminations present in flight. It is also important, when the flight data are used to validate numerical simulations, as numerical simulation are often performed on simplified geometries like canonical turret shapes on a flat plate. One source is that the aircraft fuselage, which modifies the mean incoming flow from the uniform one. Different fuselage features like the cockpit might also modify the incoming flow and the state of the boundary layer in the vicinity of the studied turret. Different realistic features of the turret itself, like the “smile” cut-outs and gaps between the moving and stationary parts of the turret will also modify the flow around the turret [3,7].

Another source of the difference is the presence of an aircraft engine just several meters downstream of the measurement station. Acoustical radiation from a loud engine will introduce strong outgoing sound waves with spatial and temporal pressure/density variations, which might introduce spurious wavefronts into the data. A similar corrupting effect of acoustic waves on atmospheric temperature measurements was studied previously [15]. The effect was observed as upstream travelling waves of a very specific frequency that appeared to propagate as a fraction of the speed of sound.

This paper will investigate this acoustically-induced wavefront error present in the flight data. This analysis is useful in that it shows that turret performance, while heavily influenced by the turret itself, is still sensitive to other aspects of the directed energy system, such as where the turret is placed relative to the aircraft engines, for this specific example. To complement this, a model will be developed using a potential flow theory. This model will be compared with the flight results to show how effective a simple acoustic model can be for predicting these aero-optic effects.

II. Experimental Setup

This experiment was performed on the Airborne Aero-Optics Laboratory-Transonic (AAOL-T). Briefly, AAOL-T Consists of two Falcon 10 aircraft flying in closed formation. One of the aircraft, designated the source aircraft, projects a 532nm diverging laser beam onto a turret mounted on the second aircraft, called the laboratory aircraft. The diverging beam overfills the 4in conformal turret aperture by a factor of 2. The turret is 12in in diameter and is hemispherical in shape. The two aircraft are flown 50m apart. The AAOL-T can fly at up to $M = 0.82$ at an altitude of 32,000 ft. A picture of the laboratory aircraft is shown in Figure 1.

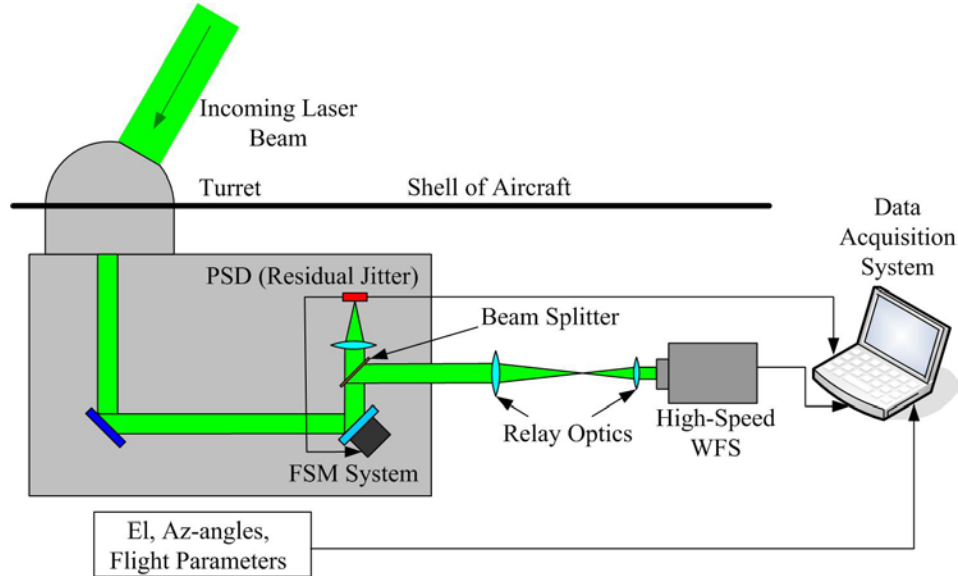


Figure 2: The optical setup and acquisition system on the AAOL. From [4].

For this flight campaign, Mach number was 0.5 and the altitude was 15,000 ft. The AAOL was instrumented with a high-speed Shack-Hartmann wavefront sensor and an angle of attack probe mounted on the opposite side of the aircraft. The optical setup is shown in Figure 2. The initial 4in beam was reduced to 0.5in on the wavefront sensor, using re-imaging optics, resulted in a 32x32 spatial resolution. The wavefronts were acquired at 25 kHz for a total of 32000 frames. Simultaneous with the wavefronts, flight conditions and the turret orientation, expressed in azimuthal (Az) and elevation (El) angles, were acquired. The data were collected with fixed relative positions between the aircrafts.

During a separate flight campaign [16], several Kulite unsteady pressure sensors were used to measure the pressure both upstream of the hemispherical turret and in its separated wake. The sensors were 10 PSI differential with a sensitivity of 0.1% of the full scale. The Kulite measurements were performed at 25 kHz for 20s. They were not performed simultaneously with the presented optical wavefronts.

III. Data Analysis

The Optical Path Difference (OPD) is the conjugate of the wavefront,

$$OPD(x, y, t) = -W(x, y, t).$$

The RMS of the OPD in space gives a measure of the beam quality at every point in time, by quantifying the wavefront's departure from a planar wavefront,

$$OPD_{RMS}(t) = \langle OPD(x, y, t)^2 \rangle_{x,y},$$

where the brackets denote averaging over the spatial coordinates. The OPD_{RMS} refers to the time-averaged RMS of the OPD,

$$OPD_{RMS} = \overline{OPD_{RMS}(t)},$$

and measures the average amount of wavefront aberrations there are at a specific viewing angle. The OPD_{RMS} is normalized by flow parameters,

$$OPD_{RMS,Norm} = \frac{OPD_{RMS}}{\rho / \rho_{SL} M^2 D},$$

where ρ is the freestream density, ρ_{SL} is the density at sea level, M is the Mach number and D is the turret diameter. This normalization has previously been shown to collapse OPD_{RMS} values across the subsonic ($M < 0.55$) flow regime [4,5,17].

Proper Orthogonal Decomposition was employed to analyze these wavefronts. POD allows the decomposition of the measured wavefronts, W , into spatial modes, ϕ_i , and temporal coefficients, a_i ,

$$W(x, y, t) = \sum_i a_i(t) \phi_i(x, y).$$

The modes are found by solving the eigenvalue problem of

$$\int C(x, y, x', y') \phi_i(x', y') dx' dy' = \lambda_i \phi_i(x, y) \text{ with } C(x, y, x', y') = \overline{W(x, y, t) W(x', y', t)}$$

and the temporal coefficients are found by taking the inner product of the modes with the wavefronts,

$$a_i(t) = \int W(x, y, t) \phi_i(x, y) dx dy.$$

The amount of optical “energy” in each mode is given by its eigenvalue, which can be computed from the temporal coefficients through

$$\lambda_n = \overline{a_n^2(t)}.$$

POD was used to isolate the acoustic modes in the wavefronts and to determine their relative importance to the other aero-optic distortions by comparing modal energies. With the acoustic-specific modes isolated, the acoustic-only wavefront can be reconstructed by only summing the acoustic-related modes back together. POD has been extensively used in both fluids and aero-optics research [18,19,20].

The turret azimuthal (Az) and elevation (El) angles were recast into angles that are more generally useful from a flow physics perspective, the viewing angle, α , and the modified elevation angle, β . The relationships between these angles and the azimuthal and elevation angles are

$$\alpha = \cos^{-1}(\cos(Az)\cos(El)) \text{ and } \beta = \tan^{-1}\left(\frac{\tan(El)}{\sin(Az)}\right).$$

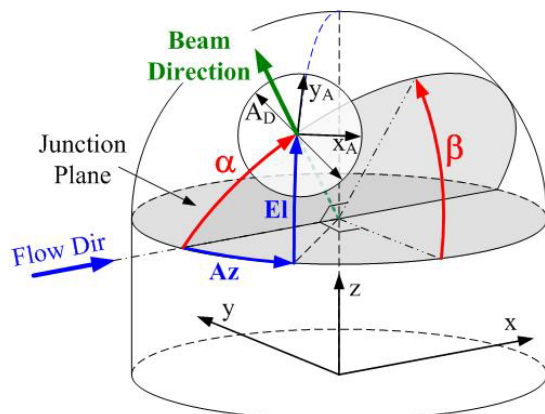


Figure 3: The relationship between the azimuthal (Az) and elevation (El) angles and the viewing (α) and modified elevation (β) angles. The turret aperture frame of reference is also shown. From [4].

The relationship between the angles is also shown in Figure 3. The aperture frame of reference is also shown in Figure 3, and all wavefront data presented in this abstract will be rotated into the turret frame of reference.

IV. Results

1. Statistical and POD Analysis

Two cases will be analyzed in the following sections. The spatial distributions of the temporal variance of OPD, is defined as $S(x_A, y_A) = \overline{(OPD^{Norm}(x_A, y_A; t))^2}^{1/2}$ where (x_A, y_A) are points over the aperture, see Figure 3 and are the overbar denotes time-averaging. The distributions for these cases, $\alpha = 88^\circ, \beta = 37^\circ$ and $\alpha = 85^\circ, \beta = 66^\circ$, are shown in Figure 4. Both are very near to directly side-looking angles. At these angles, there aren't any substantial aero-optic contributors, as the flow is attached over the aperture and the boundary layer is relatively thin. These distributions don't show any substantial difference between the two angles. The $\alpha = 88^\circ, \beta = 37^\circ$ case is slightly more energetic with the higher OPD_{RMS} , but the overall shape is similar. They also don't have any regions features that would indicate that they are atypical of the flow regime at this angle. Further, the OPD_{RMS} values are in line with what has been previously observed on the AAOL [6]. From just looking at the data statistics, despite the modified elevation angle difference, the cases are fairly similar.

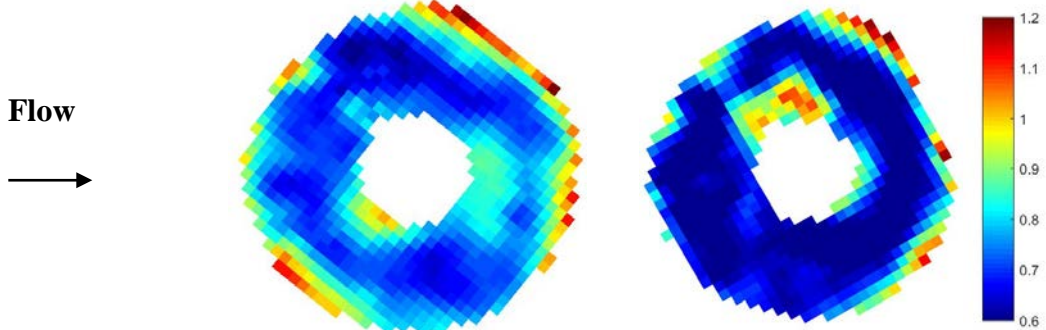


Figure 4: The spatial distribution of the temporal variance of OPD at $\alpha = 88^\circ, \beta = 37^\circ$, left and $\alpha = 85^\circ, \beta = 66^\circ$, right. The normalized average OPD_{RMS} value for the left case is $0.79 \mu\text{m}/\text{m}$ and the value for the right case is $0.71 \mu\text{m}/\text{m}$. Both cases are at $M = 0.5$. Flow direction indicated.

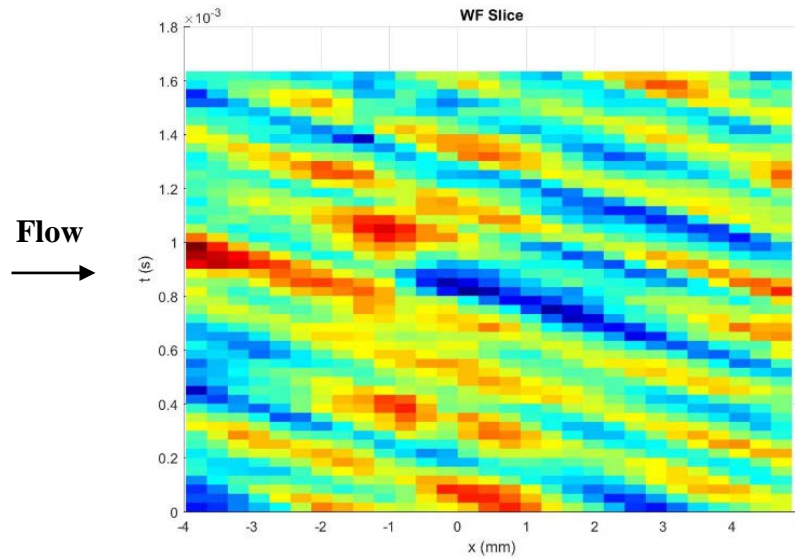


Figure 5: A one-dimensional slice of the wavefronts at $\alpha = 88^\circ, \beta = 37^\circ$ and $M = 0.5$. Flow direction is indicated. Upstream traveling waves are clearly seen as inclined regions.

A spatial-temporal plot of one-dimensional wavefront slice is shown in Figure 5. The upstream travelling wavefronts can be clearly seen, supporting the claim that these wavefronts are due to acoustic waves travelling upstream from the aircraft engine.

When POD is applied to the data cases, the difference between them becomes more apparent. Three of the first four POD modes for $\alpha = 88^\circ$, $\beta = 37^\circ$ are shown in Figure 6. These three modes are very similar in structure and energy distribution. They are the most energetic modes with this particular mode shape. All three of them have a very periodic and almost spanwise-uniform structure with a similar spatial wavelength and just differ in phase. The spatial wavelength for these modes is 0.034 m. Moreover, these modes were found to travel *upstream*. Such large, regular period structures are not expected from boundary layer aero-optic distortions as the structure size in the thin boundary layer over the aperture is small and the structures aren't as correlated or regular as these modes show. These three modes contribute almost 40% of the optical energy in this case and are by far the most dominant feature in the wavefronts.

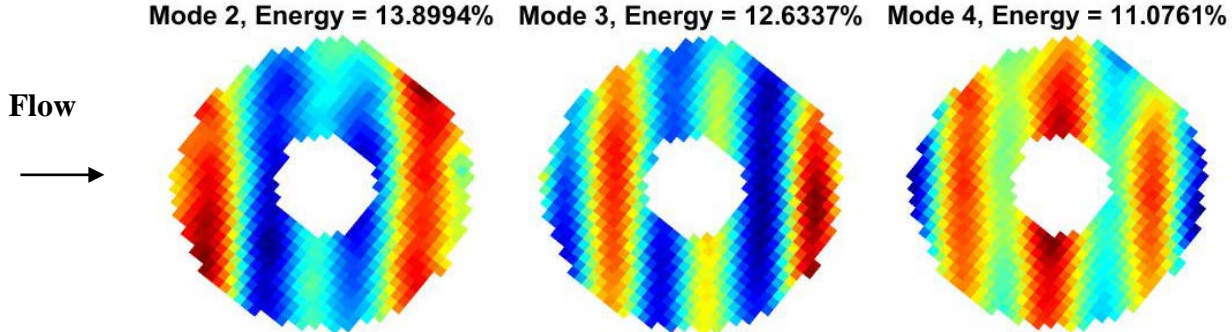


Figure 6: Modes 2-4 for $\alpha = 88^\circ$, $\beta = 37^\circ$ at $M = 0.5$. The flow direction is indicated. The modes have a spatial wavelength of $\lambda = 0.0339\text{m}$

To compare with the modes for a different angle of $\alpha = 88^\circ$, $\beta = 37^\circ$, three modes from $\alpha = 85^\circ$, $\beta = 66^\circ$ are shown in Figure 7. As was shown in Figure 6, these are the first 3 modes with the observed periodic structure. The structure is still similar to the structures observed at $\alpha = 88^\circ$, $\beta = 37^\circ$ in Figure 6, but it isn't as ordered nor as energetic. For this angle, the total energy contribution of these three modes is 6.4%, or almost an order of magnitude difference for $\alpha = 88^\circ$, $\beta = 37^\circ$ case. The spatial wavelength, though harder visually to determine from these less ordered modes, appears to be the same as the one to the one for $\alpha = 88^\circ$, $\beta = 37^\circ$ case. The difference in the POD mode strengths between these two cases indicates that the phenomenon causing this ordered structure in the wavefronts is sensitive to the aperture viewing angle, primarily α .

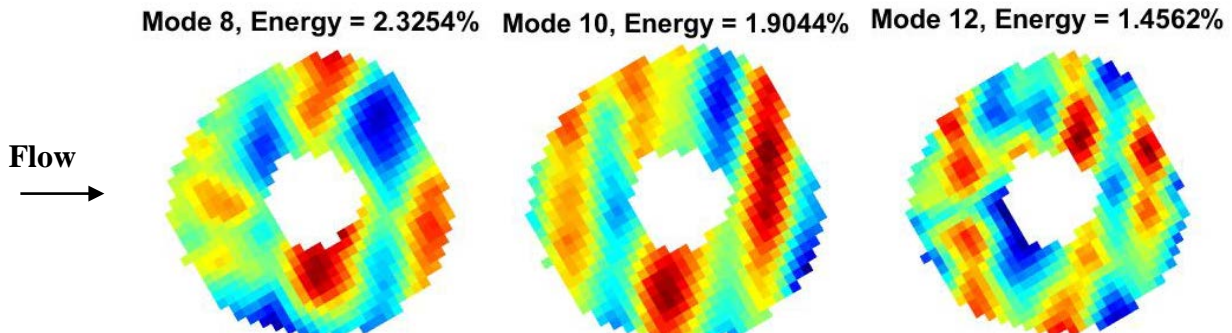


Figure 7: Modes 8, 10 and 12 for $\alpha = 85^\circ$, $\beta = 66^\circ$ at $M = 0.5$. The flow direction is indicated.

As the structures are fairly spanwise uniform and travel upstream, one possible source of these aberrations is acoustic waves travelling upstream from the aircraft engine. A schematic diagram of this is shown in Figure 8. For simplicity, the engine is modelled as a point source of periodic spherical acoustical disturbances. As the flow is subsonic, these acoustical waves, indicated as curved solid lines in Figure 8, travel upstream and reach the turret. Using this diagram, it is possible to explain the angular dependence, observed in Figures 6 and 7. When looking directly in the sideway direction from the turret ($\alpha = 90$ degrees), similar to the case in Figure 6, the optical distortions are the result of integrating through a large portion of the spherical wave with almost a constant phase. This would result in well-defined peaks and valleys in the optical signal with a strong periodic structure in the resulting wavefronts. If the viewing angle is changed by a small amount to look in the forward direction, the laser would propagate through

many acoustical waves with varying phases, so the net wavefront error is close to zero. The proposed model is consistent with the experimental observations, discussed before, when changing the viewing angle even slightly, from $\alpha = 88$ degrees in Figure 6 to $\alpha = 85$ degrees in Figure 7, resulted in a significantly reduced magnitude and periodic nature of the wave structure. As a consequence, this simplified model predicts that there's a narrow band of angles where these acoustic waves can be detected and an even narrower range in which they are the dominant source of wavefront error.

2. Convective Speed Estimate

To further provide prove that these distortions are caused by acoustic waves travelling upstream from the engine, the convective velocity magnitude of the traveling structure were determined. From Figure 5 one can see that the optical structure moves in the upstream direction and it is possible to put bounds on the values of the convective speed. Assuming a uniform freestream field, with the aircraft travelling at $M = 0.5$, the upstream-propagating acoustical wave would have a maximum velocity of $U_c = (c - M \cdot c) = 0.5c$, where c is the speed of sound, or $U_c = 160$ m/s. But since the flow accelerates near the turret to approximately 1.5 of the freestream speed, or to $0.75c$ at $M = 0.5$, the minimum expected convective velocity should be $U_c = (c - 0.75c) = 0.25c$, or $U_c = 80$ m/s.

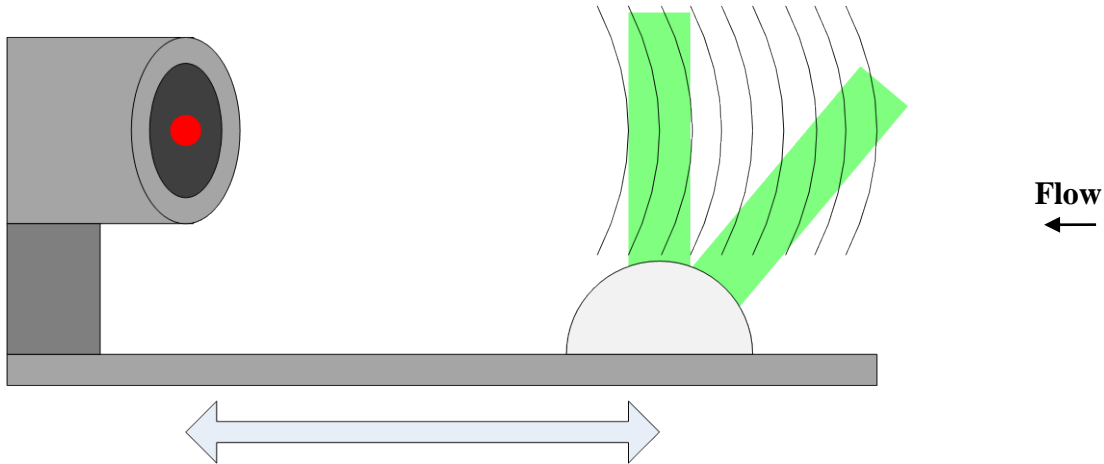


Figure 8: A diagram explaining an observed strong angular dependence of the wavefront distortion caused by an acoustic wave propagating upstream from the engine. The distance between the engine and the turret is 4.35 m. Flow direction is indicated.

Two different methods of computing the convective speed were used. First, the direct method was used, correlating two frames with a given time delay, dt , between them,

$$\text{Corr}(dx, dt) = \sum_{x, y} WF(x, y, t) \bullet WF(x + dx, y, t + dt)$$

and finding the spatial offset, dx , that provides the maximum correlation. To increase accuracy, the average correlation over all frames is computed. The peak of the correlation curve should be parabolic in shape, so a least squares parabola is fit to the correlation to provide the best estimate for the peak location. This is shown in Figure 9.

With the location of peak correlation computed, dx , the convective velocity is then given by

$$U_c = dx/dt.$$

Further, this is done across several dt 's and a linear fit between dx and dt is computed. This is shown in Figure 10. For this method, the computed convective velocity was found to be 107.6 m/s, which falls right into the expected range between $U_c = 80$ m/s and $U_c = 160$ m/s.

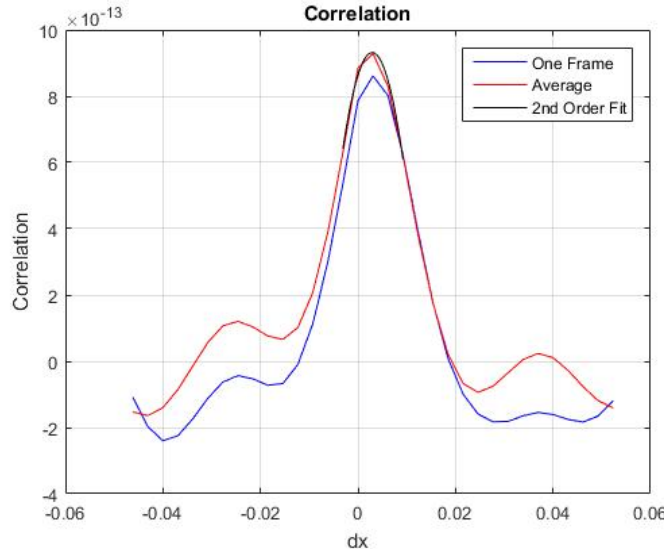


Figure 9: The correlation for $\alpha = 88^\circ$, $\beta = 37^\circ$ case at $M = 0.5$ with a time delay of one frame. The correlation of a single frame pair, the average correlation across all frame pairs and the parabolic fit to the peak are all shown.

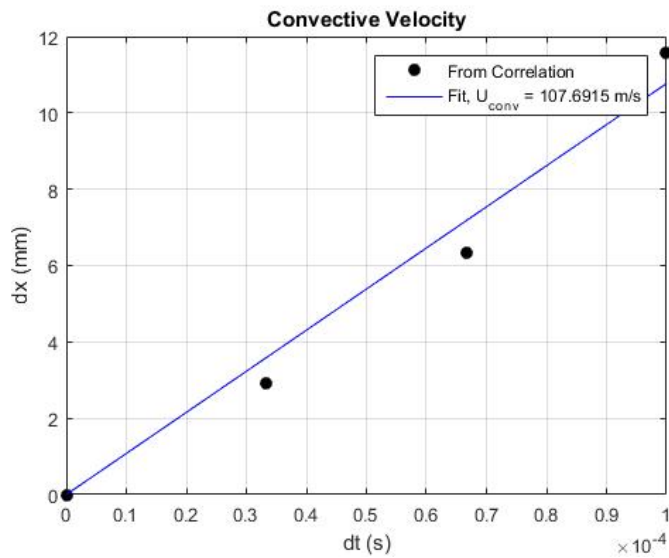


Figure 10: The convective velocity as computed by the direct method.

The second method of computing the convective velocity is to assume the structure is a travelling wave with well-defined spatial and temporal frequencies. The time series and spectra for the one of the POD modes from $\alpha = 88^\circ$, $\beta = 37^\circ$ case is shown in Figure 10. The time series in Figure 11, left, shows that the mode is very periodic in nature with a well-defined frequency. By computing the spectra, Figure 11, right, the frequency of the traveling structure was determined to be $f = 4717$ Hz. As was established in Figure 5, the modes have a spatial wavelength, λ , of 0.034 m. The convective velocity can then be computed as

$$U_c = \lambda f$$

Using this equation, the convective speed was found to be $U_c = 159$ m/s, different from the first estimate, though still within the expected range. The waves moving upstream at $U_c = c(1-M)$ was observed in [15] as well.

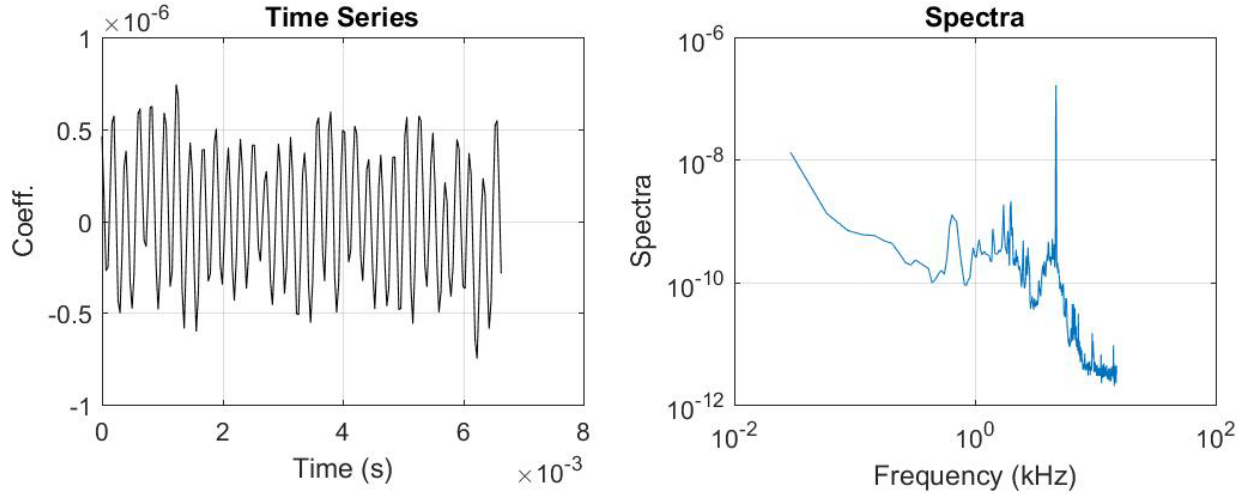


Figure 11: The time series (left) and spectra (right) for the temporal coefficient of Mode 3 of the 88° , $\beta = 37^\circ$ case. For this case, $M = 0.5$ and the POD mode that corresponds to these spectra is shown in Figure 5, middle. The spectral peak is $f = 4717$ Hz.

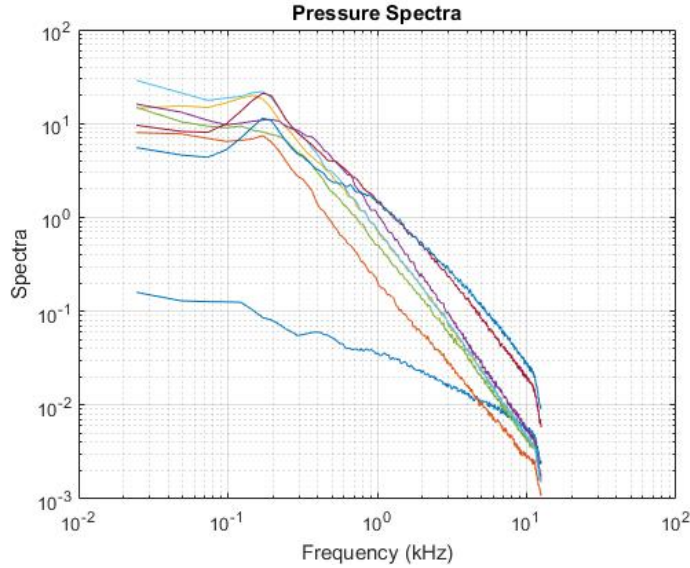


Figure 12: Pressure measurements obtained near the turret in flight.

Figure 12 shows the pressure spectra measured near the turret in flight on the AAOL [16]. The spectra were taken from several Kulite sensors in the wake and upstream of the turret. The pressure spectra do not show any discernable peak at 4717 Hz, which was observed in the wavefront modal spectra. This indicates that the pressure fluctuations due to this acoustic mode are relatively small compared to the sensitivity of the sensor used. As mentioned in Experimental Setup section, a 10 PSI differential Kulite sensor was used, and it has a sensitivity of $\pm 0.1\%$ of its full scale. This means that it is insufficient for measuring fluctuations below 70 Pascals. Assuming that 70 Pascals is the lower limit on the amplitude that could be measured with it, any acoustic behavior below an $SPL=20*\log(70Pa / 20 \mu Pa) = 130$ dB is undetectable. This means that the observed acoustic phenomenon must be weaker than that at the turret location. It is due to the integrated nature of the measurement and the acoustical signal been in phase along the beam at side-looking angles, as well as high sensitivity of the wavefront sensor we were able to detect this acoustic behavior.

3. Acoustic Modelling

As shown in Figure 8, the phenomenon observed in the wavefronts was also modelled as a travelling acoustic source. The model predicts acoustical field along x-y plane, with the x-axis being in the streamwise direction, going through the hemisphere center with positive x pointing upstream and the y-axis being in the airplane surface normal

direction, with positive y pointing outward from the aircraft. The model assumes that flow is purely in the x -direction with a Mach number, M . It also uses the incompressible potential flow around a sphere to estimate the flow field around a turret. Finally, it assumes that the acoustic noise is purely from a point source and that the density fluctuations due to the acoustic source are adiabatic. The source is located downstream of the turret at $x = -4.35$ m and away from turret center at $y = 0.5$ m.

The pressure field [21] from the acoustic source is given by

$$p(R, \theta; t) = \frac{1}{4\pi} \frac{q[t - (R/c)]}{R(1 - M \cos \theta)^2} + \frac{q}{4\pi} \frac{(\cos \theta - M)U}{R^2(1 - M \cos \theta)^2}.$$

where c is the speed of sound and U is the freestream velocity. The amplitude, A , and frequency, $f = 4717$ Hz, of the acoustic source are contained in q and its derivative,

$$\begin{aligned} q(t) &= A \sin(2\pi ft) \\ q'[t - (R/c)] &= 2\pi f A \cos(2\pi f(t - R/c))' \end{aligned}$$

R is given by

$$R = \frac{R_1}{1 - M \cos \theta} \text{ with } R_1 = \sqrt{(x - Ut)^2 + (1 - M^2)y^2}.$$

and, θ is defined as the angle between the source and the observation point, or with source at the origin,

$$\theta = \tan^{-1}(y/x).$$

The full derivation for a travelling acoustic source using potential flow theory is available in [21].

As mentioned before, the turret was modeled as a sphere with an incompressible potential flow around it [22]. The velocity field around the sphere is given by

$$u_r = U \cos \theta_t \left(1 - \frac{R_t^3}{r_t^3} \right) \text{ and } u_\theta = -U \sin \theta_t \left(1 + \frac{R_t^3}{2r_t^3} \right).$$

Here u_r and u_θ are the radial and angular velocity components around the turret and r_t and θ_t are the distance from the turret and the angle about the turret. The radius of the turret is R_t . As we're only assuming flow in the x -direction, it is helpful to recast these velocity components into the x - y coordinate system:

$$u_x = u_r \cos \theta_t - u_\theta \sin(\theta_t) \text{ and } u_y = u_r \sin \theta_t + u_\theta \cos(\theta_t).$$

We can use the x -component of the velocity field to define the entire velocity field of our system.

To combine the two models into a single predictive model for our system, we need to re-define the acoustic model to account for the non-constant Mach number field near the turret. The key to this step is acknowledging that the Mach number of the acoustic model simply gives the phase of the pressure fluctuation at each spatial location. Because the sound waves travel through a velocity field with varying Mach numbers as they approach the turret, to find the correct phase at a given point, the average Mach number along a line between the acoustic source and the point in the flow field must be found,

$$\overline{M} = \frac{\int M(x, y) dl}{\int dl}.$$

Here, dl is the differential path length between the acoustic source and the point in the flow. If Mach number at each point in the flow field is known, the entire acoustic pressure field can be computed. With the acoustic field computed, the SPL can be computed from the amplitude of the pressure fluctuations at a given location because they are sinusoidal in time. Additionally, by assuming an adiabatic process, the density field can be obtained through

$$\frac{p}{p_0} = \left(\frac{\rho}{\rho_0} \right)^{1.4}.$$

This density can be integrated along the beam path and combined with the Gladstone-Dale constant, K_{GD} , for air to obtain the optical path difference, OPD :

$$OPD = \int K_{GD} \rho'(x, y) dl,$$

where the integration occurs along the beam path. This is the quantity directly measured in flight.

The model was tuned using the actual in-flight fluid parameters and the measured wavefront at $\alpha = 88^\circ$. In particular, the source strength was tuned to match the OPD_{RMS} at that point, as there are no relevant pressure measurements to fit the model to, as shown in Figure 12. The source strength was chosen such that the OPD_{RMS} from the model at that angle matched the measured OPD_{RMS} from the wavefronts. The solution was computed for various beam grids at different viewing angles. Each beam grid was 500x10000 points and 50 m in length from the turret center. As computing the line integrals to get the effective Mach number was the most computationally intensive step, a separate grid with all of the effective Mach numbers was pre-computed. The effective Mach numbers of the beam grids were found by interpolating onto the beam grids. This simulation was carried out on 211 different beam grids, equally spaced from $\alpha = 45^\circ$ to $\alpha = 150^\circ$.

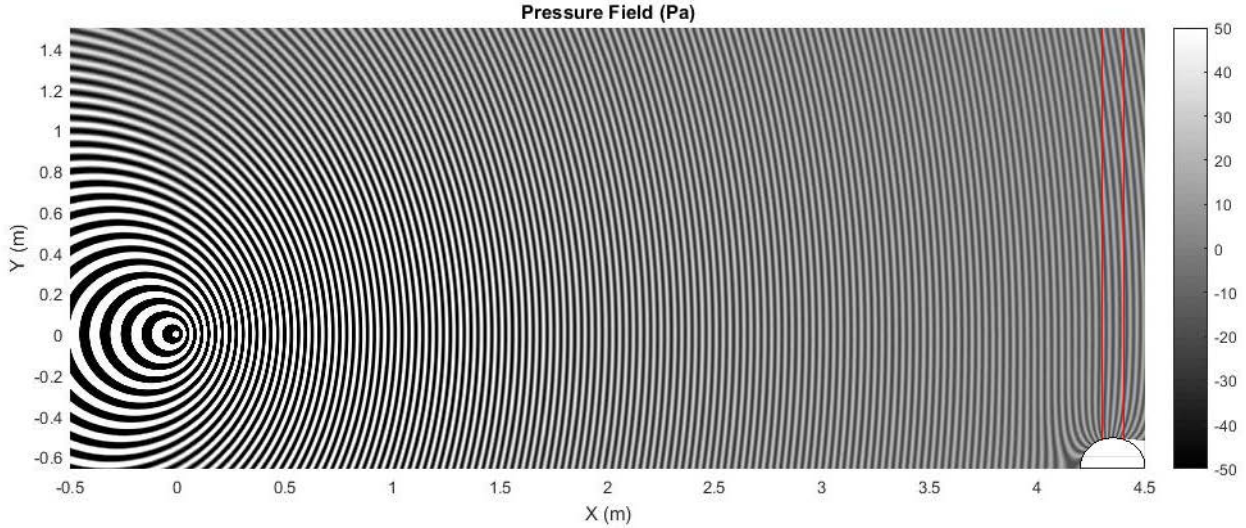


Figure 13: The pressure field from the model. Flow goes right to left. The red lines indicate the integrated beam path. The pressure is shown in Pascals.

The full pressure field from the model is shown in Figure 13. There are several features that serve as sanity checks on the model. First, the pressure field away from the turret displays the expected behavior of a moving source, as the spatial wavelength is decreased in front of the source and decreased behind it. With the source moving at $U_C = 0.5c$, we expect the wavelength upstream of the source, to the right of the plot, to be decreased by a factor of 2, and we expect it to be increased by a factor of 1.5 downstream, which is what we observe in Figure 13. Second, the pressure fluctuation magnitude is decreasing radially away from the source, also as expected for an acoustic source. Finally, the presence of the turret only changes the pressure field in the very near region to the turret itself. This is further shown in Figure 14, where a zoomed-in pressure field around the turret is shown. Very near the turret, the acceleration of the flow causes the acoustic waves to further decrease in spatial wavelength, as the local speed approaches $U_C = 0.75c$. Near the downstream portion of the turret, as the flow decelerates to $M = 0$ at the stagnation point, the spatial wavelength increases as the pressure waves can move faster relative to the local flow. Without the turret model, Figure 14 right, there is no variation in the phase of the pressure waves around the turret at all, as expected.

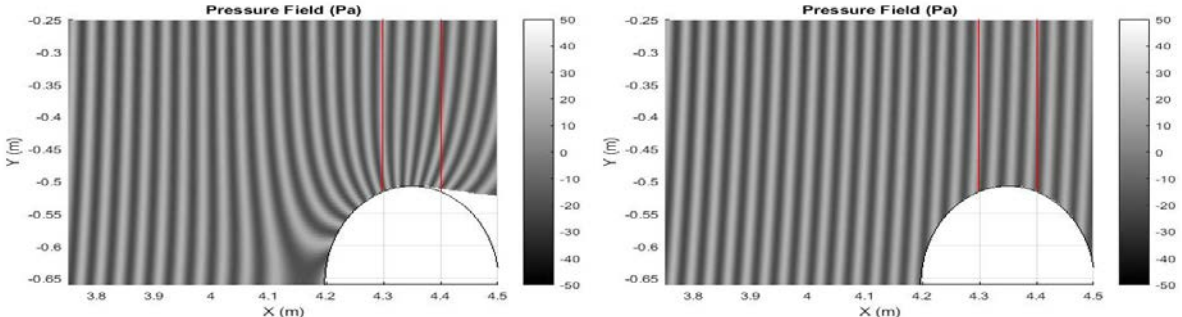


Figure 14: The model near the turret. Left is with the turret velocity field modeled, right is without. Flow goes right to left. The pressure is shown in Pascals.

The SPL can also be computed from the model at every point via

$$SPL = 20 \log_{10} \left(\frac{P_{rms}}{20 \mu Pa} \right) \text{ (in dB).}$$

This is shown as a function of distance upstream of the acoustic source in Figure 15. The SPL falls off at 20 dB per decade, as expected. The peak SPL near the engine is almost 170 dB, and the SPL at the turret (4.3m upstream) is approximately 116 dB. This value near the turret is lower than the predicted maximum SPL from the unsteady pressure data obtained on the aircraft. Note that the included turret model doesn't actually affect the SPL at all as all it does is modify the local phase of the pressure fluctuations due to the source, not the amplitude of those waves. So, if only the SPL levels are of interest, a simple model with the uniform freestream, shown in Figure 14, right, can be used.

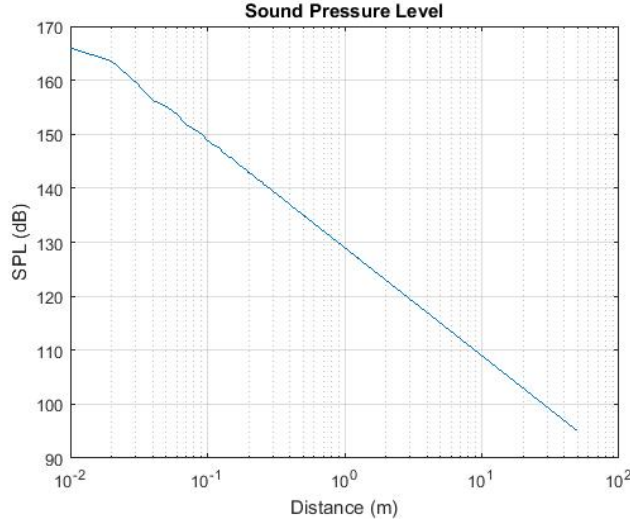


Figure 15: The sound pressure level as a function of distance upstream from the source.

4. Model Comparison and Predictions

The OPD_{RMS} as a function of the viewing angle as predicted from the model is shown in Figure 16, left. As shown, the model agrees quite well with the measured OPD_{RMS} values from the data discussed previously. The integrated wavefronts also match the experimentally-measured wavefronts, as shown in Figure 16, right. Thus, the model predicts both the wavelength and magnitude very well, and as a consequence, the model also correctly predicts the convective velocity. For the measured frequency of 4717 Hz, and using $U_c = \lambda f$, the same convective speed is found, $U_c = 159$ m/s. This corresponds to a convective velocity of exactly 0.5c.

The model predicts a very low OPD_{RMS} for forward-looking angles below $\alpha = 85^\circ - 90^\circ$. This is due to the integrated nature of the optical distortions. The total OPD_{RMS} at a given angle is dependent on the amount of in-phase density that the beam integrates through along the beam path; the longer the in-phase region, the larger the wavefront aberrations. Integrating through an in-phase region along the beam path adds to the OPD because the density fluctuations are all the same sign. Conversely, integrating through alternating in-and-out of phase regions will effectively cancel each other out. This behavior is shown in Figures 17 and 18. For $\alpha = 75^\circ$, Figure 17 left, the total in-phase region that is integrated through is very small, only within the first quarter meter or less of propagation. This results in a relatively small amplitude for the wavefront, as shown in Figure 18. For $\alpha = 85^\circ$, Figure 17 middle, the in-phase density region is much longer, being effectively the first half meter or more. As the beam integrates through a longer region of in-phase density, the amplitude of the wavefront aberration increases and the OPD_{RMS} increases accordingly. This is further shown at $\alpha = 90^\circ$, Figure 17 right, where the laser path is actually tangent to the propagation direction of the acoustic waves. There's about a meter or more of in-phase density that is propagated through.

The location of in-phase density also determines the measured convective velocity using the wavefronts. The local flow Mach number is a function of the distance from the turret. The region that contributes the most to the wavefront, while close to the turret, is far enough away that the local velocity is very close to the freestream velocity. Due to this, measured and model-predicted wavefronts near $\alpha = 90^\circ$ both give a convective velocity of 0.5c.

The model predicts that the acoustic contribution to the wavefront stays relatively constant as a function of viewing angle larger than $\alpha = 90^\circ$, as shown in Figure 16. This is because at all angles less than $\alpha = 90^\circ$, the wavefronts

are integrating through a similar-size region of in-phase density. The largest contribution to the wavefronts occurs when integrating along a region of in-phase density in the beam direction. This occurs when the beam is directly normal to the propagating direction of the acoustic waves. As the laser beam looks further back, the beam still eventually integrates through a region where the propagation direction of the acoustic waves is directly normal to the direction of the beam, as can be seen in Figure 19. At $\alpha = 105^\circ$, the beam propagates through a region where the density phase is changing for the first 1.5-2m. Then, it integrates through an in-phase region very similar to what was observed at $\alpha = 90^\circ$, just further down the beam path. Because the wavefronts are an integrated quantity, it does not matter where the in-phase region occurs. This occurs for nearly all angles at $\alpha > 90^\circ$; the location of the in-phase region just changes as a function of the viewing angle.

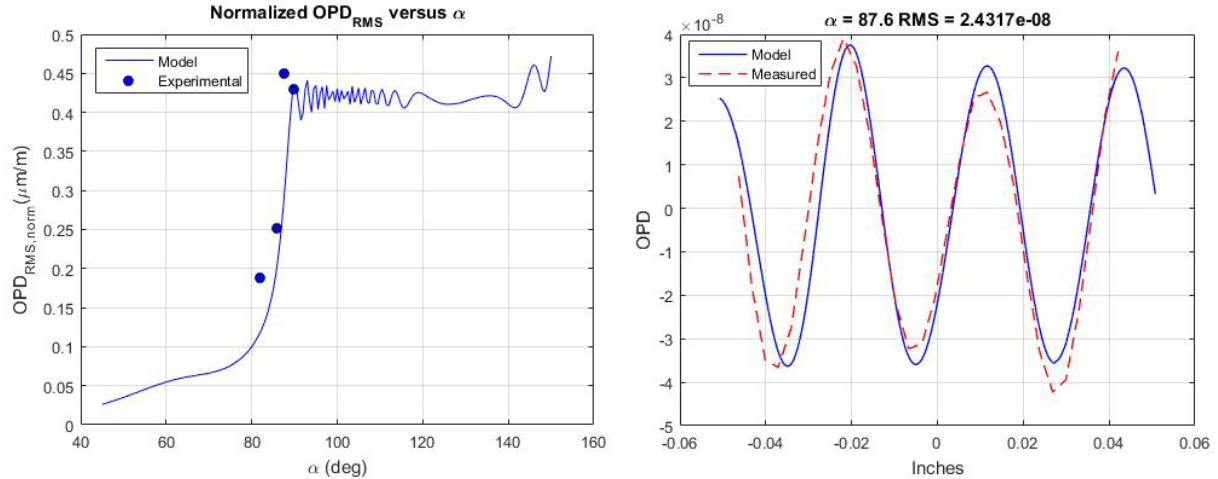


Figure 16: The OPD_{RMS} from the model as a function of viewing angle, left. The blue circles are the experimental data points. Left is with the turret model, right is without. The integrated wavefronts from the model compared with real wavefronts, right.

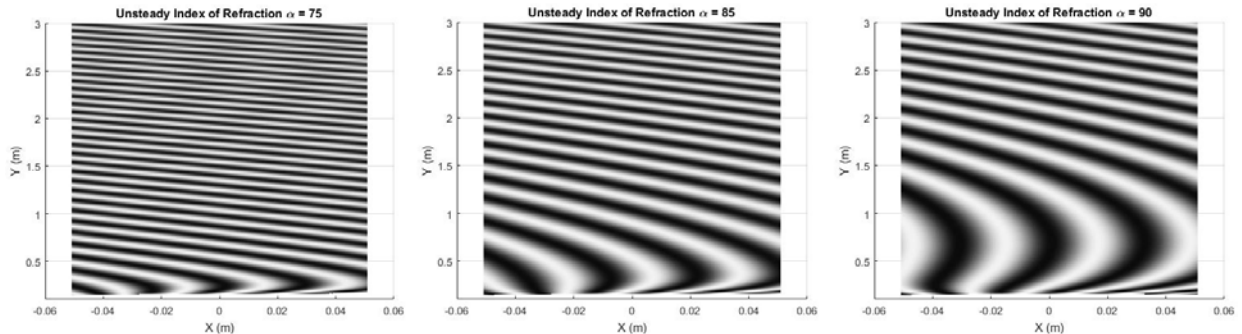


Figure 17: The index of refraction field along the beam for $\alpha = 75^\circ$, left, $\alpha = 85^\circ$, middle and $\alpha = 90^\circ$, right.

In reality, the acoustic phenomenon hasn't been readily observed in downstream-looking wavefronts for two primary reasons. First, the assumption that the acoustic source is purely a point source with no obstructions besides the turret breaks down as α increases. From Figure 1, it can be seen that the turret has relatively direct line-of-sight with the engine, which lets the acoustic waves travel un-impeded to the regions right around the turret. Further away, however, the engine housing begins to block-off-sight with the engine itself, and violating the spherical source assumption in the model. This will likely impede the path of the acoustic waves. Essentially, the further the in-phase region of density is from the turret, the more likely it will be disrupted by the presence of the engine housing. This potentially has an effect of decreasing the acoustic contribution to the wavefronts as α increases. Second, the relative strength of the acoustic contribution to the wavefronts and other flow-related contributions will change for increasing α . The normalized OPD_{RMS} for $M = 0.5$ [23] is shown in Figure 20. At $\alpha = 90^\circ$, the only other contribution to the wavefronts is a relatively thin boundary-layer, which has fairly weak aero-optical distortions at subsonic speeds. For $\alpha > 105^\circ$, the normalized OPD_{RMS} of the flow is nominally between 2 and 6 due to the separated wake behind the aircraft [4,5,6], which is much larger than the peak normalized OPD_{RMS} from the phenomenon of 0.5. Looking very

far forward, the acoustic wavefront contribution as predicted by the model falls below the noise floor of the sensor. Essentially, right near $\alpha = 90^\circ$ is the only region where the acoustic waves are strong enough to be detected and not overshadowed by stronger aero-optic phenomena.

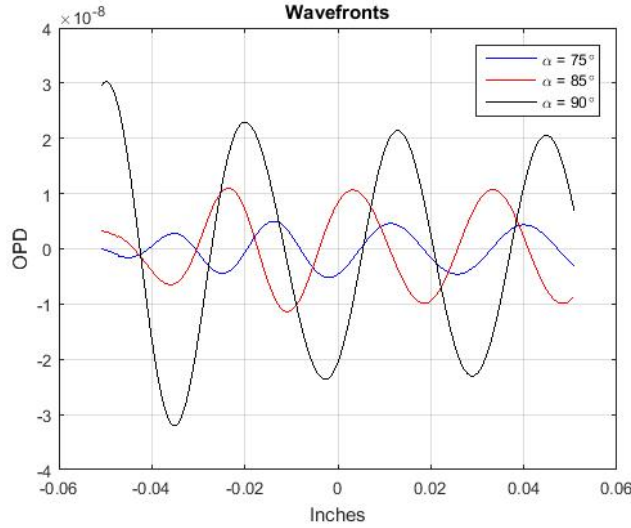


Figure 18: The model-predicted wavefronts at $\alpha = 75^\circ$, $\alpha = 85^\circ$ and $\alpha = 90^\circ$, left.

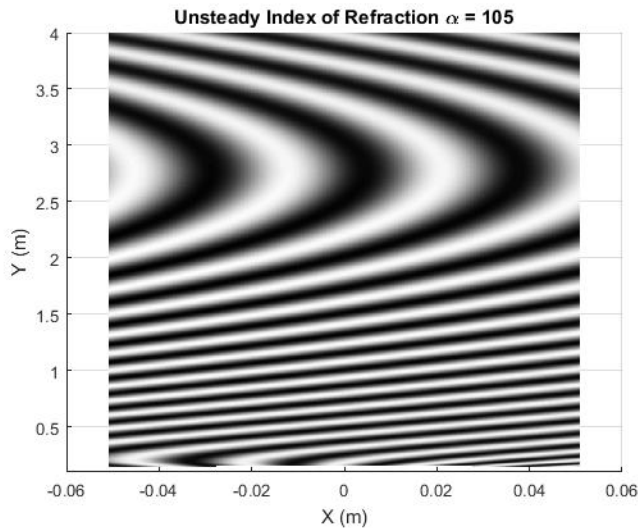


Figure 19: The unsteady index of refraction field for $\alpha = 105^\circ$. Here, the X and Y coordinates centered on the turret center.

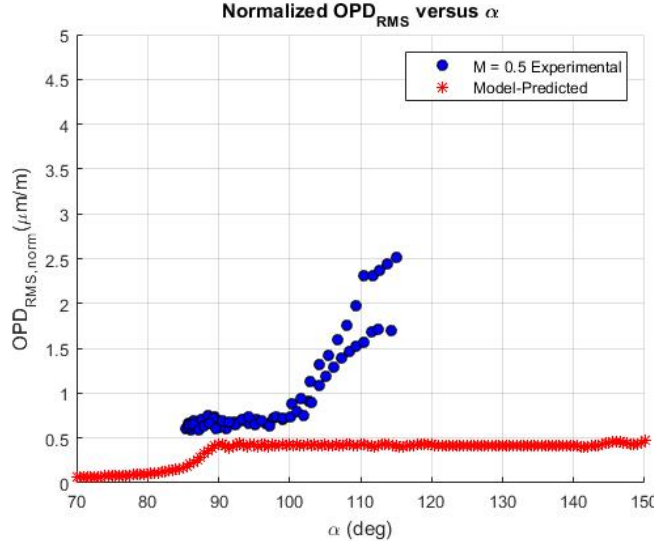


Figure 20: The normalized OPD_{RMS} as a function of viewing angle, both experimental values and due to acoustics only, predicted by the model. Experimental Data from [23].

V. Conclusions

An acoustic-related phenomenon was observed in wavefront data on the AAOL. The phenomenon was shown to have a strong angular dependence and consist of very periodic spanwise-uniform structures travelling upstream. It was observed in two different cases of wavefront data at $M = 0.5$. The convective speed of the waves was computed using two different methods and was bounded between $U_c = 107$ m/s and $U_c = 159$ m/s. Based on it travelling upstream, the source of the acoustic waves is most likely the aircraft engine. Additionally, unsteady pressure spectra for Kulites placed near the turret showed that the maximum possible SPL from the engine at the turret would be 130 dB.

A simple point-source model was developed to simulate the measured acoustic noise. This model is based on the potential flow solution for a moving acoustic source. The local velocity field around the turret was approximated as a flow around a sphere. This model was used to compute the SPL field between the acoustic source and the turret. By matching the acoustical-only wavefronts with the model-predicted ones, SPL near the turret was estimated to be 116 dB.

The model was compared with experimental data near $\alpha = 90^\circ$ and showed really good agreement. It correctly predicted both the wavefront spatial wavelength and OPD_{RMS} . Because the temporal frequency of acoustic source was set based on the wavefront measurements and the model predicted the spatial frequency properly, the convective velocity was also predicted to be the same as measured in the wavefronts.

The model showed that the majority of the wavefront error induced by the acoustic waves comes from integrating through a region where the density field along the laser beam is in-phase; this region is where the acoustic waves are travelling directly perpendicular to the laser beam propagation direction. Outside of that region, acoustic waves are out of phase, with the resulted contributing wavefront error being near zero. As a consequence, the wavefront contribution from acoustic waves for looking-forward angles $\alpha < 90^\circ$ is small. For back-looking angles $\alpha > 90^\circ$ the model predicts that the acoustic-related wavefront error should remain relatively constant. However, due to the engine housing affecting the directivity of the acoustic waves in practice, the model is expected to fail for large α .

Acknowledgments

This work is supported by the Joint Technology Office, Grant number FA9550-13-1-0001. The U.S. Government is authorized to reproduce and distribute reprints for governmental purposes notwithstanding any copyright notation thereon.

References

- [1] Snyder, C.H., Franke, M.E., Masquelier, M.L., "Wind-Tunnel Tests of an Aircraft Turret Model", Journal of Aircraft, 37(3), pp. 368-376, 2000.
- [2] Sluder, R., Gris, L., Katz, J., "Aerodynamics of a Generic Optical Turret", Journal of Aircraft, 45(5), pp. 1814-1815, 2008.

- [3] Gordeyev, S., De Lucca, N., Jumper, E.J., Hird, K., Juliano, T.J., Gregory, J.W., Thordahl, J., and Wittich, D.J., "Comparison of Unsteady Pressure Fields on Turrets with Different Surface Features using Pressure Sensitive Paint", *Experiments in Fluids*, 55, p. 1661, 2014.
- [4] Porter C., Gordeyev, S., Zenk, M. and Jumper, E.J., "Flight Measurements of the Aero-Optical Environment around a Flat-Windowed Turret", *AIAA Journal*, 51(6), pp. 1394-1403, 2013.
- [5] De Lucca, N., Gordeyev, S., and Jumper, E.J., "In-flight aero-optics of turrets", *Journal of Optical Engineering*, 52(7), 071405, 2013
- [6] J. Morrida, S. Gordeyev and E. Jumper, "Transonic Flow Dynamics Over a Hemisphere in Flight", AIAA Paper 2016-1349, 2016.
- [7] E. Mathews, K. Wang, M. Wang and E. Jumper, "LES of an Aero-Optical Turret Flow at High Reynolds Number", AIAA 2016-1461, 2016.
- [8] R. Jelic, S. Sherer and R. Greendyke, "Simulation of Various Turret Configurations at Subsonic and Transonic Flight Conditions Using OVERFLOW", *Journal of Aircraft*, 50, pp. 398-409, 2013.
- [9] Coirier, W.J., Porter, C., Barber, J., Stutts, J., Whiteley, M., Goorskey, D. and Drye, R., "Aero-Optical Evaluation of Notional Turrets in Subsonic, Transonic and Supersonic Regimes," AIAA Paper 2014-2355, 2014
- [10] P.E.Morgan and M.R. Visbal, "Hybrid Reynolds-Averaged Navier-Stokes/Large-Eddy Simulation Investigating Control of Flow over a Turret," *Journal of Aircraft*, Vol. 49, No. 6, pp. 1700-1717, 2012.
- [11] Ladd, J., Mani, A. and Bower, W., "Validation of Aerodynamic and Optical Computations for the Unsteady Flow Field About a Hemisphere-on-Cylinder Turret," AIAA Paper 2009-4118, 2009.
- [12] Jumper, E.J., Zenk, M., Gordeyev, S., Cavalieri, D., and Whiteley, M., "Airborne Aero-Optics Laboratory", *Journal of Optical Engineering*, 52(7), 071408, 2013.
- [13] E.J. Jumper, S. Gordeyev, D. Cavalieri, P. Rollins, M.R. Whiteley and M.J. Krizo, "Airborne Aero-Optics Laboratory - Transonic (AAOL-T)", AIAA Paper 2015-0675, 2015.
- [14] N. De Lucca, S. Gordeyev and E. Jumper, "The Improvement of the Aero-Optical Environment of a Hemisphere-on-Cylinder Turret using Vortex Generators", AIAA Paper 2013-3132, 2013.
- [15] Hugo R.J., Nowlin S.R., Hahn I.L., Eaton F.D., McCrae K.A., "Acoustic Noise-Source Identification in Aircraft-Based Atmospheric Temperature Measurements," *AIAA Journal*, 40(7), pp. 1382-1387, 2002.
- [16] J. Morrida, S. Gordeyev and E. Jumper, "Simultaneous Pressure and Optical Measurements Around Hemispherical Turret in Subsonic and Transonic Flight," AIAA Paper 2017-3654, 2017.
- [17] Gordeyev, S., and Jumper, E.J., "Fluid Dynamics and Aero-Optics of Turrets", *Progress in Aerospace Sciences*, 46, pp. 388-400, 2010
- [18] Berkooz, G., Holmes, P., & Lumley, J. L. "The proper orthogonal decomposition in the analysis of turbulent flows," *Ann. Rev. Fluid Mech.*, 25, pp. 539-575, 1993.
- [19] Holmes, P., Lumley, J. L., & Berkooz, G., *Turbulence, Coherent Structures, Dynamical Systems and Symmetry*, Cambridge University Press, 1996.
- [20] Lumley, J., *Stochastic Tools in Turbulence*, Academic, New York, 1970.
- [21] Morse P. M. and Ingard K. U., *Theoretical Acoustics*, Princeton University Press, 1968.
- [22] Joseph D. Funada T. and Wang J., *Potential Flows of Viscous and Viscoelastic Liquids*. Cambridge Aerospace Series. 2007.
- [23] J. Morrida, S. Gordeyev, N. De Lucca, E. Jumper, "Shock-Related Effects on Aero-Optical Environment for Hemisphere-On-Cylinder Turrets at Transonic Speeds," *Applied Optics*, 56(16), pp. 4814-4824, 2017.